


Converting CO₂ to formic acid by tuning quantum states in metal chalcogenide clusters

Turbasu Sengupta ¹✉ & Shiv N. Khanna ¹✉

The catalytic conversion of CO₂ into valuable chemicals is an effective strategy for reducing its adverse impact on the environment. In this work, the formation of formic acid via CO₂ hydrogenation on bare and ligated Ti₆Se₈ clusters is investigated with gradient-corrected density functional theory. It is shown that attaching suitable ligands (i.e., PMe₃, CO) to a metal-chalcogenide cluster transforms it into an effective donor/acceptor enabling it to serve as an efficient catalyst. Furthermore, by controlling the ratio of the attached donor/acceptor ligands, it is possible to predictably alter the barrier heights of the CO₂ hydrogenation reaction and, thereby, the rate of CO₂ conversion. Our calculation further reveals that by using this strategy, the barrier heights of CO₂ hydrogenation can be reduced to ~0.12 eV or possibly even lower, providing unique opportunities to control the reaction rates by using different combinations of donor/acceptor ligands.

¹Department of Physics, Virginia Commonwealth University, Richmond, VA 23284-2000, USA. ✉email: senguptat@vcu.edu; snkhanna@vcu.edu

The rapid increase of the CO₂ level in the atmosphere has become a serious concern to mankind in recent times^{1,2}. One of the direct solutions to the problem is utilizing porous or mesoporous adsorbents as a medium for CO₂ capture³. However, the high cost associated with storage and transport restricts such procedures from large-scale industrial applications⁴. As an alternative, the conversion of CO₂ into useful chemicals represents a relatively cost-effective strategy^{4–6}. Aside from reducing CO₂ concentration in the atmosphere, the converted products can also be utilized as a resource for value-added chemicals. Among the assortment of chemicals that CO₂ can be chemically converted into, formic acid (FA) represents a compelling choice for a multitude of reasons^{7–9}. As a chemical, formic acid is extensively used as feedstock material and can also be transformed into value-added products with relative ease. As an energy-dense material, it can also be used as an alternative to fossil fuels, thereby being effective in reducing the carbon footprint. Additionally, having a high volumetric hydrogen density, it also has immense potential as an effective hydrogen storage vector⁸. At room temperature, formic acid is a low-toxic liquid; therefore, the storage and transportation of formic acid are significantly cost-efficient. As a result of these advantages, a significant amount of worldwide CO₂ conversion is now performed in the form of formic acid, and the net conversion quantity is rising at a rapid pace every year^{4,8}.

One of the major challenges of converting CO₂ to formic acid is the inherent inertness of CO₂. Being thermodynamically and kinetically stable¹⁰, CO₂ hydrogenation without an effective catalyst is a difficult task under normal conditions. Nowadays, a range of homogeneous and heterogeneous catalysts are available for CO₂ hydrogenation, and the reaction can be carried out thermochemically or electrochemically as required^{11–18}. One of the focuses of this current paper is to evaluate the potential of the metal chalcogenide clusters (e.g., Ti₆Se₈) toward thermochemical CO₂ conversion to formic acid. In recent times, ligated metal chalcogenide clusters have gained considerable attention due to their high stability and ease of synthesis in a solvent medium^{19–23}. These stable ligated clusters can also be assembled as ionic solids with complementary units like fullerenes. In the past decades, significant numbers of such clusters and assemblies have been experimentally synthesized by Roy, Nuckolls, and coworkers^{20–25}. In such solids, the ligand-protected cluster cores usually act as charge donors, whereas the fullerene moieties are charge acceptors, resulting in extended three-dimensional ionic crystals that are similar in structure to CdI₂ or NaCl. Incidentally, it was also shown^{26–33} that within such solids, the ligated clusters maintain their chemical identity, and the attached ligands control the donor/acceptor characteristics of the clusters, providing a unique opportunity to predictably alter the properties of the whole superstructure altogether.

Historically, ligands have always played a pivotal role in cluster chemistry^{34–37}. Apart from protecting the sensitive cluster core or preventing a cluster from coalescence or leaching, they can also be utilized to electronically stabilize a metal cluster by filling up the valence shell to the nearby magic number. In some rare instances, it was observed that ligands could also enhance the reactivity of a cluster via the formation of localized active sites or donor-acceptor pairs^{38–41}. In that regard, the effect of ligands on the electronic structure of the metal chalcogenide cluster is observed to be unique. It has been shown^{26–33} that by controlling the number and type of the attached ligands, one can transform a metal chalcogenide cluster into a strong electron donor or an acceptor by shifting the whole electronic spectrum without altering the valence shell configuration. For example, we have shown that strong σ -donor ligands like phosphines induce an upward shift of the electronic spectrum, whereas a shift in the

reverse direction is noticed for strong π -acceptor ligands like CO. The overall effect of the ligands in such cases can be conceptualized as a Coulombic well that surrounds the cluster core and thereby influencing the discrete energy levels of the cluster.

In the present paper, we have considered Ti₆Se₈ as a model cluster catalyst and investigated its catalytic potential toward formic acid synthesis via CO₂ hydrogenation. Our calculation of the minimum energy pathway reveals that in comparison to other reported catalysts, the unligated Ti₆Se₈ cluster is a really good catalyst for CO₂ hydrogenation with significantly low barrier heights ranging from ~ 0.3 – 0.4 eV^{42–44}. However, what sets the Ti₆Se₈ cluster apart from any conventional catalyst, is not the lower barriers for hydrogenation but rather the dependence of the barrier heights on the attached ligands. Controlling the rate of a chemical reaction has always remained an elusive goal for chemists and materials scientists. However, apart from a few exceptional examples, reports of such achievements are rare. Among the notable examples, controlling reactivity by microwave irradiation⁴⁵ is observed earlier for an electron transfer reaction. Recently, Pan and Liu⁴⁶ have shown an interesting example where control of chemical reactivity is achieved by Fermi-coupled vibrational states. In this work, we show that a similar goal can also be achieved by ligated Ti₆Se₈ clusters simply by varying the number and type of the attached ligands. It is observed that attaching π -acceptor ligands, e.g., CO, to the cluster results in an increase of hydrogenation barriers compared to pristine Ti₆Se₈, whereas σ -donor ligands like PMe₃ reduce the barriers for the reaction. Thus, by selectively controlling the ratio of attached acceptor and donor ligands to the cluster, one can increase or decrease the barrier heights for CO₂ hydrogenation in a stepwise manner. Our calculation further indicates that by attaching only 3 PMe₃ ligands to the cluster, one of the CO₂ hydrogenation barriers can be reduced to as low as 0.12 eV. Investigation of the electronic structure of the ligated clusters proves that the alteration of the barrier heights is due to the ligand-induced shift in the electronic levels. The upward shift of the electronic levels by PMe₃ facilitates the electron transfer as well as energetically destabilizes the cluster-hydrogen bond and assists the release of H atom(s) and, thereby, the reaction. An opposite effect hinders the reactivity when one or more CO ligands are introduced. Thus, we have shown that apart from protecting the cluster core, ligands can also be utilized as a tool for controlling the reactivity of the cluster. In regard to that, our current investigation offers a simplistic, cost-efficient, and easily achievable approach to the problem.

Results

Calculation of the reaction pathway of CO₂ → HCOOH conversion on the Ti₆Se₈ cluster. To investigate the catalytic potential of the metal chalcogenide cluster toward CO₂ hydrogenation, we have chosen the Ti₆Se₈ cluster as our template catalyst. In previous investigations, titanium-doped nanoparticles and surfaces have shown remarkable promises and performances toward CO₂ reduction reactions^{47–50}. Our choice of Ti₆Se₈ cluster is influenced by such experimental and theoretical results. It is noteworthy that although the specific Ti₆Se₈ cluster reported in this paper is not yet reported experimentally, similar metal chalcogenide clusters with identical stoichiometric compositions are chemically synthesized^{20–25}. The optimized ground state geometry of Ti₆Se₈ is a distorted face-capped octahedron with 0 μ_B spin magnetic moment. Figure 1a shows the ground state optimized geometry of the Ti₆Se₈ cluster along with some bond lengths (in Å). The structure with 2 μ_B spin magnetic moment is ~ 0.14 eV higher in energy compared to the ground state geometry (see Supplementary Table 1). The HOMO-LUMO gap, adiabatic

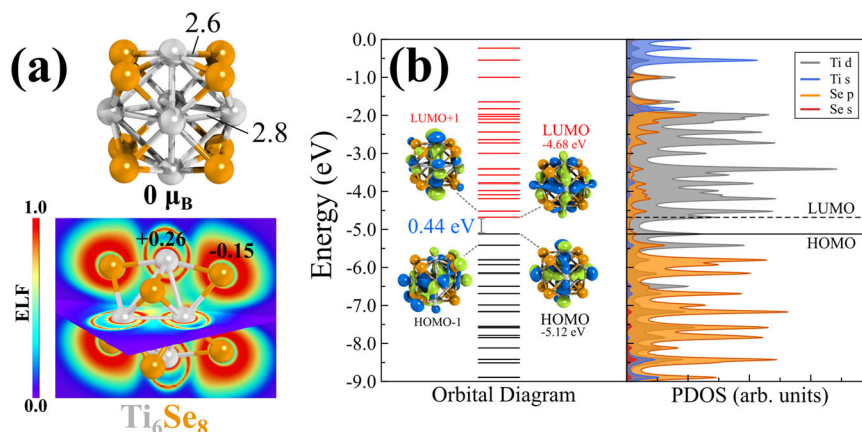


Fig. 1 Structure and electronic properties of Ti_6Se_8 cluster. **a** Ground state optimized structure of Ti_6Se_8 cluster (bond distances are in Å) and the contour plot of the electron localization function (ELF) along with the Hirshfeld charges on the Ti and Se atoms (**b**) the molecular orbital (MO) and the projected density of states (PDOS) diagram of Ti_6Se_8 cluster. Isosurfaces of a few important orbitals are also shown.

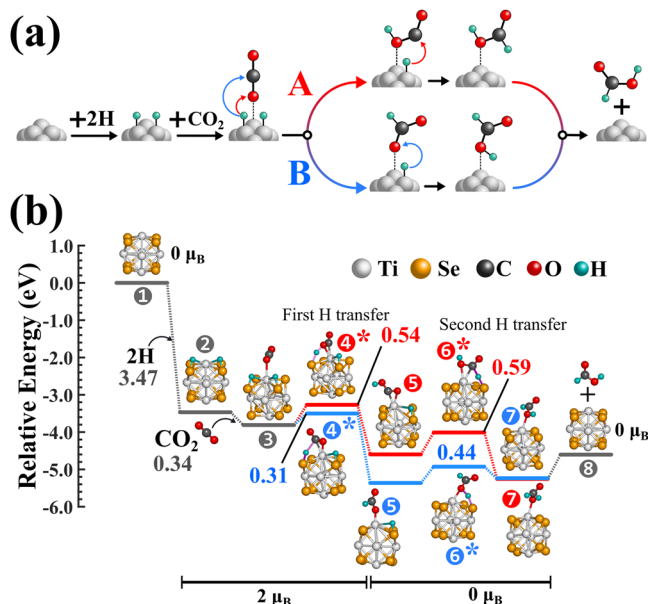


Fig. 2 $\text{CO}_2 \rightarrow \text{HCOOH}$ conversion pathways. **a** The schematic of $\text{CO}_2 \rightarrow \text{HCOOH}$ conversion on a cluster surface showing two possible reaction pathways (A and B) and **b** the computed reaction pathways on the ground state Ti_6Se_8 cluster. The binding energies of H and CO_2 are shown in grey, barrier heights of the two pathways (A and B) are shown in red and blue color, respectively. The transition states are marked with asterisk (*) symbol.

ionization energy (AIE), and adiabatic electron affinity (AEA) of the ground state ($0 \mu_B$) cluster are 0.44, 6.79, and 2.98 eV, respectively. Electron localization function (ELF) calculation (Fig. 1a) further reveals that the electrons are mostly localized on the Se atoms, which also explains the observed negative Hirshfeld⁵¹ charge ($-0.15 |e|$) on the selenium atoms. In contrast, the Ti atoms are seen to be positively charged ($+0.26 |e|$). The projected density of states (PDOS) and the molecular orbital (MO) diagram of the cluster is included in Fig. 1b. The PDOS diagram and the frontier orbital isosurfaces clearly show that both the HOMO and LUMO are composed of Ti-d orbitals, and Se has minor contributions.

As a next step, we proceed to compute the favorable reaction pathway of CO_2 hydrogenation on the Ti_6Se_8 cluster catalyst.

Figure 2a shows a general schematic of the $\text{CO}_2 \rightarrow \text{HCOOH}$ conversion on a cluster surface. For the present study, we have considered that the first step of the reaction is the adsorption of dissociated H atoms on the cluster surface, which is followed by the adsorption of a CO_2 molecule at an adjacent site of the cluster. Our calculation (see Supplementary Fig. 1) reveals that the H_2 dissociation barrier on the Ti_6Se_8 cluster is 1.08 eV (PBE/TZ2P); however, dissociated H atoms produced by any other experimental methods^{52–55} can also be used for the reaction as alternatives. Since the adsorption sites of CO_2 and H atoms are different, the sequence by which they are adsorbed on the cluster surface is irrelevant to the present reaction. Further discussion regarding this and related arguments, specifically for the Ti_6Se_8 cluster, is given later on. Following the adsorption steps, we have found that the reaction has the possibility to proceed via two pathways depending on to which atom of the CO_2 molecule (C or O) the first H atom gets transferred. As shown in Fig. 2a, we have designated these two pathways as (A) and (B) in red and blue color, respectively. In pathway A, the first H gets transferred to the nearest O atom of the CO_2 molecule resulting in a COOH intermediate, and subsequent transfer of the 2nd H to the C atom of the intermediate yields the formic acid. In path B, the reaction proceeds via an HCOO intermediate since the first H gets attached to the C atom of CO_2 . The formic acid is then produced via the transfer of the second hydrogen from the cluster surface to the nearest O atom of the intermediate.

In Fig. 2b, we have shown both the calculated pathways on Ti_6Se_8 clusters. As we have shown in the schematics, the first step is considered to be the adsorption of the H atoms on the cluster surface. Although we expected that the H atoms would bind only to the Ti or Se site, upon adsorption, it was noticed that the dissociated H atoms favorably formed bridging bonds with the Ti and one of the nearby Se atoms with a net binding energy of 3.47 eV. This is evident by looking into the geometric structure of intermediate 2, as shown in Fig. 2b. This is due to chalcogens like S or Se being able to form a much stronger bond with H compared to Ti. Wiberg bond indices (WBI) calculated by Natural bond orbital (NBO) analysis⁵⁶ further revealed that the Se–H bond order is significantly higher (0.82–0.85) compared to the Ti–H bond order (0.07–0.09), showing that the Se–H interaction is the dominant one. Important to note that after H adsorption, the ground state spin-only magnetic moment is also altered to $2 \mu_B$. The bridging orientation of H and stronger Se–H interaction proves two things. First, even after the adsorption of H atoms, the Ti site remains free for CO_2 adsorption. So there is

minimal competition between H and CO₂ adsorption on the cluster as long as the number of H atoms is reasonably low, and hence their adsorption order (i.e., which one among H or CO₂ is adsorbed first) does not influence the calculated reaction pathway. Second, since the interaction of the dissociated H atoms is much stronger with Se than Ti, the presence of nearby H atoms does not affect the binding energy of the incoming CO₂ at a lower H concentration. Therefore, it is expected that the reaction parameters will remain the same as long as the number of adsorbed H that are in close vicinity to CO₂ remains low. Hence, although here we have considered the whole reaction pathway by coadsorbing both the hydrogen atoms, sequential adsorption, i.e., one H atom at a time, should not alter the reaction parameters. These observations and conclusions were also confirmed in previous investigations based on the Mo₆S₈ cluster^{57,58}. It is noteworthy that the computed reaction pathways presented here are all based on the aforementioned assumptions, i.e., the number of adsorbed H atoms remains low. The influence of a higher number of adsorbed H on the reaction mechanism demands a separate study and is not the current focus of the paper. Following the H adsorption, the resulting cluster complex, i.e., intermediate 2 gets stabilized by 0.34 eV via the adsorption of CO₂ on the Ti atom. This leads to structure 3, as shown in Fig. 2b. We have observed that, in contrast to H, the CO₂ molecule prefers to bind with the Ti site via one of the O atoms. Upon adsorption, the molecule adopts an angular orientation with respect to the cluster surface.

As shown previously, starting from 3, the reaction can possibly proceed via two different pathways, namely A and B respectively. We have investigated both the pathways for Ti₆Se₈ clusters, and the barrier heights are included in Fig. 2b. From the diagram, it is seen that the two barrier heights of the first (4*) and second (6*) H transfer along pathway A (COOH intermediate, shown as red-colored 5 in Fig. 2b) are 0.54 and 0.59 eV, respectively. In contrast, the reaction pathway via the HCOO intermediate (i.e., pathway B) shows significantly lower barrier heights, 0.31 and 0.44 eV, respectively. The lowering of the second barrier height in pathway B can be attributed to the lowering of the intermediate (5) along with the transition states (6*), as shown in Fig. 2b. Due to the lower barriers, it is evident that the CO₂ → HCOOH conversion on the Ti₆Se₈ clusters will preferably proceed via pathway B and through the HCOO intermediate (blue-colored 5 in Fig. 2b) despite the energies of the final products (7 in Fig. 2b) from both pathways are near identical. The sum of energies of the free cluster and formic acid are included in the same figure as 8 for reference purposes. It is also important to note that the ground state spin moments do not remain constant throughout the reaction. A second spin alteration is noticed after the first transition state. Thus, although 2μ_B spin magnetic moment is maintained till 4*, beginning from intermediate 5 in both A and B pathways, the ground state moment has altered to 0μ_B, which remained the same till the end of the reaction. The relative energies of all species in the reaction pathway considering the different magnetic moments are provided in the Supplementary Table 2 and 3.

Effect of ligands on the reaction pathway of CO₂ → HCOOH conversion. Following the calculation of the most favorable CO₂ → HCOOH conversion route on the pristine Ti₆Se₈ cluster, we proceed to understand how ligands will influence the barrier heights of CO₂ hydrogenation. To achieve this, we have chosen two different dative ligands, namely, PMe₃ and CO. Based on the electronic effect, these two ligands differ widely from each other. The PMe₃ ligand is a strong σ-donor but a poor π-acceptor. In contrast, the CO ligand is a strong electron donor as well as a

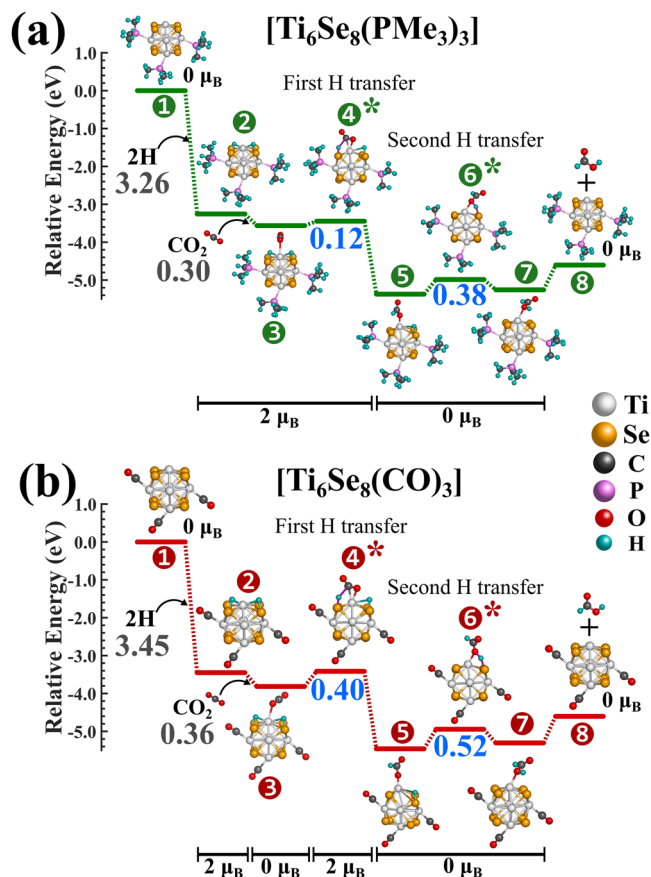


Fig. 3 CO₂ → HCOOH conversion on the Ti₆Se₈(PMe₃)₃ and Ti₆Se₈(CO)₃ clusters. The most favorable CO₂ → HCOOH conversion pathways on the (a) Ti₆Se₈(PMe₃)₃ and (b) Ti₆Se₈(CO)₃ clusters. The binding energies of H and CO₂ are shown in grey, barrier heights are shown in blue color. The transition states are marked with asterisk (*) symbol.

good π-acceptor. Starting from the pristine Ti₆Se₈, we have sequentially increased the number of attached ligands with the Ti atoms of the cluster. In all cases, we have kept the reaction site unligated so that the reaction could proceed without any hindrance. In this present work, we have restricted ourselves to a maximum of three ligands of each type. The major reason behind this is that we have observed that going beyond three ligands (especially for PMe₃) results in a major steric crowding in the vicinity of the reaction site. This results in a weakening of CO₂/H binding and subsequent desorption from the cluster surface. Our test calculation on Ti₆Se₈(CO)₃ cluster (see Supplementary Fig. 2) indicated that pathway B remains energetically favorable even after ligand attachment. Hence, for the ligated systems, only pathway B is computed and included in this study. Figures 3a, b show the reaction pathway of CO₂ → HCOOH conversion on the Ti₆Se₈(PMe₃)₃ and Ti₆Se₈(CO)₃ clusters, respectively. The results for the rest of the ligated clusters (i.e., Ti₆Se₈(PMe₃)_n and Ti₆Se₈(CO)_n, n = 1-2) are included in the Supplementary Table 4-6. As shown, the trend of the barrier heights for CO₂ hydrogenation on the ligated clusters is observed to be very interesting. As reported, for all the CO-ligated clusters, including Ti₆Se₈(CO)₃, both the CO₂ hydrogenation barriers are shown to be higher compared to the Ti₆Se₈ cluster. It is interesting to note that the first barriers for all three Ti₆Se₈(CO)_n clusters are nearly the same ~0.40 eV. However, the second barrier is observed to increase by ~0.03-0.04 eV with the increment of the number of the attached CO ligands one at a time (see Supplementary Table 6). In contrast, an opposite trend is noticed for

$\text{Ti}_6\text{Se}_8(\text{PMe}_3)_n$ clusters. All the PMe_3 attached clusters show relatively lower barrier heights compared to Ti_6Se_8 for CO_2 hydrogenation. In the case of PMe_3 ligated clusters, both the hydrogenation barriers are observed to decrease with the increment of the number of ligands attached to the cluster. However, the first hydrogenation barrier falls off more rapidly compared to the second one. In the case of $\text{Ti}_6\text{Se}_8(\text{PMe}_3)_3$ cluster (Fig. 3a), the first hydrogenation barrier was calculated as 0.12 eV, which is a significant reduction compared to that of Ti_6Se_8 (i.e., 0.31 eV). The alteration of the second CO_2 hydrogenation barrier (0.38 eV) was not as drastic as the first one, and in this case, a reduction of 0.06 eV was noticed compared to for Ti_6Se_8 cluster (0.44 eV). As shown in Fig. 3, upon analyzing the relative energies of all the chemical species, we have observed the overall reduction of the second hydrogenation barrier in the case of $\text{Ti}_6\text{Se}_8(\text{PMe}_3)_3$ cluster compared to $\text{Ti}_6\text{Se}_8(\text{CO})_3$ is due to the energetic lowering of the transition state (6^*) as well as due to the energetic destabilization of the respective intermediate (5). Both of these factors simultaneously result in a lower second hydrogenation barrier for the $\text{Ti}_6\text{Se}_8(\text{PMe}_3)_3$ cluster. At this point, it is important to mention that we have observed that using a hybrid functional (e.g., PBE0) instead of PBE is altering the barrier heights marginally (see Supplementary Fig. 3). Therefore, it is expected that even with a different level of theory, the relative trends and the conclusions drawn herewith will still remain the same.

So far, we have shown that the barrier heights of CO_2 hydrogenation on Ti_6Se_8 can effectively be decreased/increased by decorating the cluster with σ -donor (e.g., PMe_3) or π -acceptor (e.g., CO) ligands. This provides a unique opportunity to predictably alter the reactivity of a cluster simply by changing the ratio of the attached ligands of both types. To further elaborate on this possibility, we started from the $\text{Ti}_6\text{Se}_8(\text{PMe}_3)_3$ cluster and sequentially replaced one PMe_3 with one CO ligand at each step till we reached $\text{Ti}_6\text{Se}_8(\text{CO})_3$ cluster. The reaction profiles of these two intermediate clusters, i.e., $[\text{Ti}_6\text{Se}_8(\text{PMe}_3)_{3-m}(\text{CO})_m]$ ($m = 1, 2$) clusters along with all the optimized geometries are shown in Fig. 4. The relative energies of all species in the reaction pathway considering the different magnetic moments of $[\text{Ti}_6\text{Se}_8(\text{PMe}_3)_{3-m}(\text{CO})_m]$ ($m = 1, 2$) clusters are included in the Supplementary Tables 7–8. As expected, both the barrier heights of these two clusters are observed to be intermediate in magnitude compared to the barrier heights obtained for the $\text{Ti}_6\text{Se}_8(\text{PMe}_3)_3$ and $\text{Ti}_6\text{Se}_8(\text{CO})_3$ clusters (Fig. 3). In Fig. 5, we have combined the barrier heights of both hydrogenation steps for all these four ligated clusters, i.e., $[\text{Ti}_6\text{Se}_8(\text{PMe}_3)_{3-m}(\text{CO})_m]$ ($m = 0-3$), and as shown, it is now evident that by sequentially changing the ratio of the attached PMe_3 and CO ligands, both the hydrogenation barriers can be altered in a controlled and stepwise manner. The range of alteration in the first and second barriers at each step is observed to be 0.07–0.13 and 0.02–0.10 eV, respectively. It is important to mention that by observing the stepwise reduction of barrier heights, one can argue that some of the barrier height differences between the adjacent step are not that significant considering the error range of the DFT methodology; however, it is impossible to ignore the observed systematic trend as the Fig. 5 show a near-smooth decrease of both the hydrogenation barriers as we sequentially increase the number of attached PMe_3 ligands. This observation is crucial since, by using such strategies, it might be possible for experimentalists to predictably alter and control the rate of a particular reaction and hence the reactivity of the cluster. Moreover, by using a larger cluster with more available sites for ligand attachment and by using a stronger donor, the magnitude of stepwise barrier height reduction can further be increased. Additionally, it is noteworthy that although the stepwise reduction in barrier height for the present cluster may be low

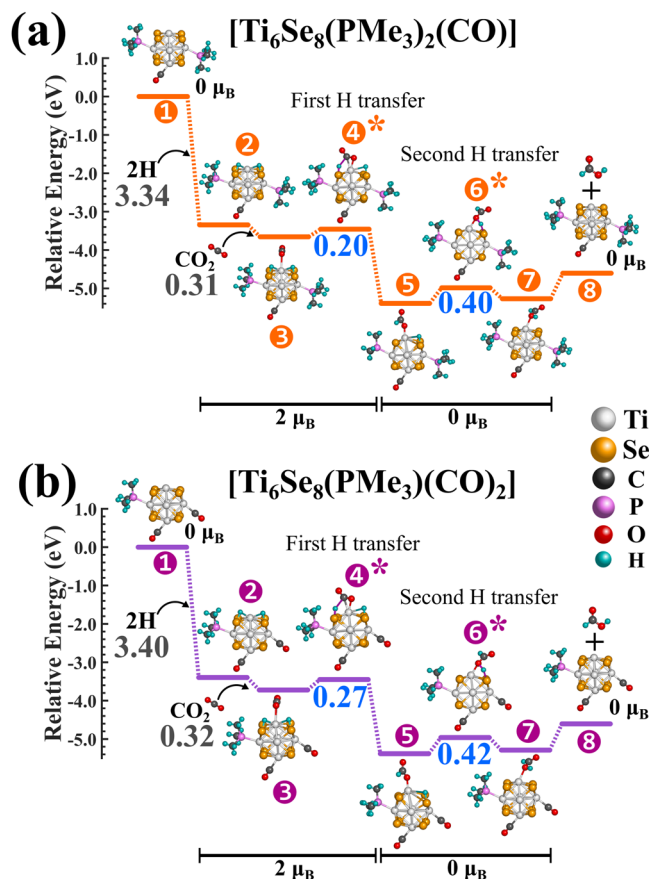


Fig. 4 $\text{CO}_2 \rightarrow \text{HCOOH}$ conversion on the $[\text{Ti}_6\text{Se}_8(\text{PMe}_3)_{3-m}(\text{CO})_m]$ ($m = 1, 2$) clusters. The most favorable $\text{CO}_2 \rightarrow \text{HCOOH}$ conversion pathways on the (a) $\text{Ti}_6\text{Se}_8(\text{PMe}_3)_2(\text{CO})$ and (b) $\text{Ti}_6\text{Se}_8(\text{PMe}_3)(\text{CO})_2$ clusters. The binding energies of H and CO_2 are shown in grey, barrier heights are shown in blue color. The transition states are marked with asterisk (*) symbol.

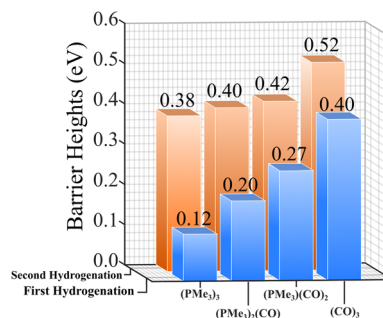


Fig. 5 Ligand-induced barrier heights of $\text{CO}_2 \rightarrow \text{HCOOH}$ conversion. The relative trend of the barrier heights for both the hydrogenation steps of $[\text{Ti}_6\text{Se}_8(\text{PMe}_3)_{3-m}(\text{CO})_m]$ ($m = 0-3$) clusters. The plot shows smooth predictable alteration of barrier heights upon ligand substitution.

in some cases, the overall reduction of the hydrogenation barrier heights (0.14–0.28 eV, considering both hydrogenation steps) from $\text{Ti}_6\text{Se}_8(\text{CO})_3$ to $\text{Ti}_6\text{Se}_8(\text{PMe}_3)_3$ cluster is reasonably significant.

Understanding the ligand-induced reactivity alteration of the Ti_6Se_8 cluster toward CO_2 conversion. We now consider the underlying electronic effects that are responsible for such

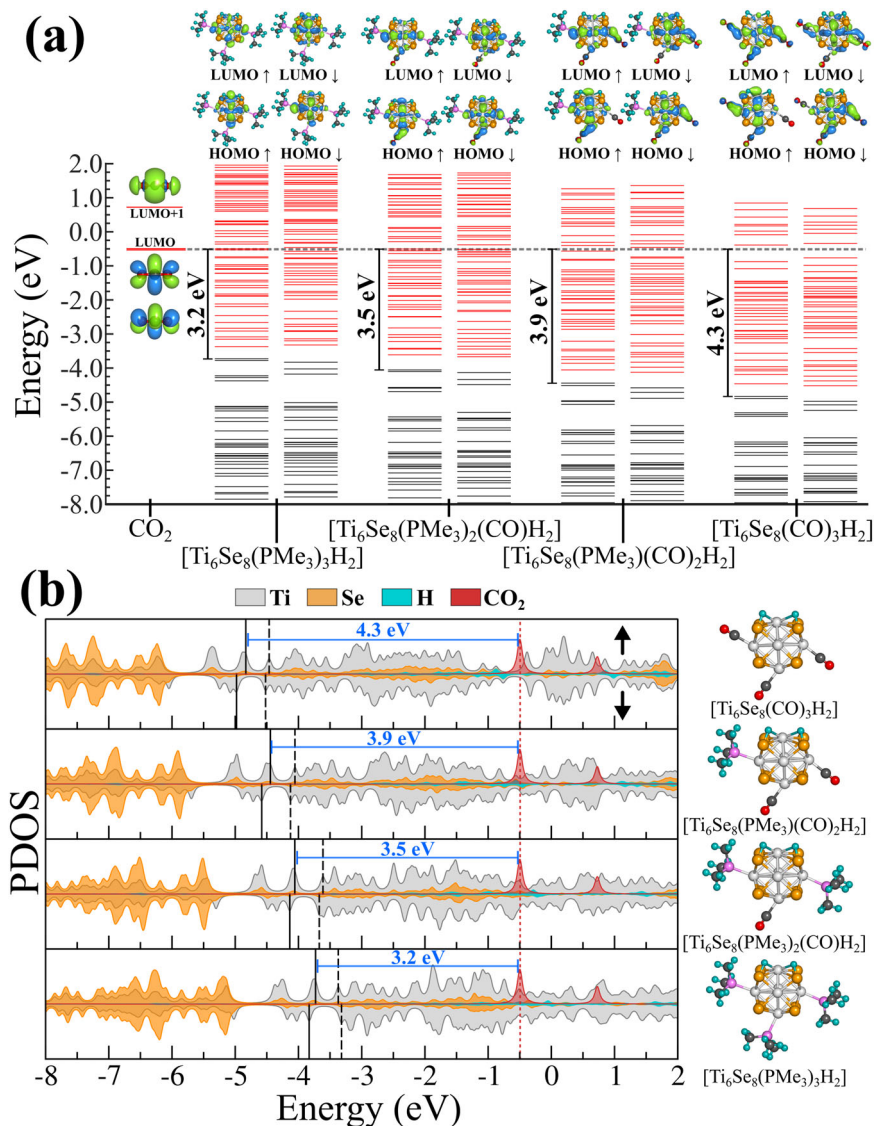


Fig. 6 Ligand induced electronic property alteration of intermediate 2. **a** Molecular orbital (MO) and **b** projected density of states (PDOS) diagram of intermediate 2 for the $[\text{Ti}_6\text{Se}_8(\text{PMe}_3)_{3-m}(\text{CO})_m]$ ($m = 0-3$) cluster. The black and red lines in **a** represents the occupied and unoccupied levels. In **b**, the location of HOMO and LUMO for each spin channel is marked by solid and dashed black lines respectively. The LUMO of CO_2 molecule is indicated by a dashed red line.

alteration of the reactivity of the clusters. To achieve this, we have plotted the molecular orbital (MO) diagram and the projected density of states (PDOS) (Fig. 6) of intermediate 2 for the four ligated clusters. An alternative version of the same figure, along with the electronic structure of Ti_6Se_8 cluster, is included in the Supplementary Fig. 4. As shown earlier (Figs. 3 and 4), intermediate 2 is obtained via the adsorption of the H atoms on the cluster surface, and hence it can be considered one of the crucial species in the reaction pathway. From Fig. 6, we can see that increasing the number of PMe_3 ligands at each step (right to left for **6a** and top to bottom for **6b**) creates an energetical upward shift of the whole electronic (MO) spectrum of intermediate 2. This shift is observed for both spin channels of intermediate 2 with minimal alteration in the HOMO-LUMO gaps of the same. It is noteworthy that the upward shift has also not perturbed the order of molecular orbitals or the occupation number of both spin channels (intermediate 2). In Fig. 6, we have also included the MO diagram and PDOS of a free CO_2 molecule for reference purposes. The ligand-induced upward energetic shift of intermediate 2 results in the alteration of multiple important

properties. First, the upward shift of the electronic (MO) spectrum results in the reduction of the energetic gap between the HOMO of intermediate 2 and LUMO of the free CO_2 molecule, thereby favoring the orbital overlap and the charge transfer during the course of the reaction. As one can see from Fig. 6, the respective gap is considerably lower, i.e., 3.2 eV for $[\text{Ti}_6\text{Se}_8(\text{PMe}_3)_3\text{H}_2]$ cluster compared to 4.3 eV as obtained for $[\text{Ti}_6\text{Se}_8(\text{CO})_3\text{H}_2]$ cluster. Additionally, due to the ligand-induced upward shift of the electronic (MO) spectrum, intermediate 2 also becomes a better electron donor due to the reduction in the ionization energy. In Fig. 7, we have shown the trends in the ionization energy of intermediate 2 for all four clusters. As depicted, the adiabatic ionization energy (AIE) of the $[\text{Ti}_6\text{Se}_8(\text{PMe}_3)_3\text{H}_2]$ is observed to be significantly lower (5.08 eV) compared to the AIE of the $[\text{Ti}_6\text{Se}_8(\text{CO})_3\text{H}_2]$ cluster (6.34 eV) which further facilitates the charge transfer from the intermediate 2 to CO_2 . This argument can also be proven simply by looking at the accumulated charges on the CO_2 molecule at the first transition state (i.e., 4^* in Figs. 3 and 4). The Hirshfeld⁵¹ charge on CO_2 at the respective transition state is more negative ($-0.36 |e|$) in the

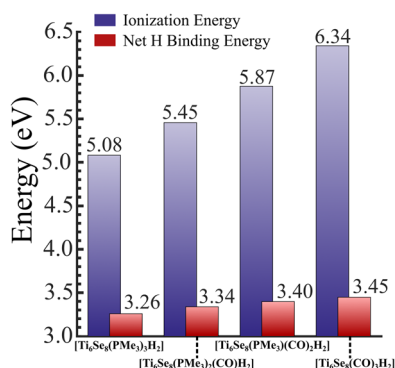


Fig. 7 Ligand-induced alteration of AIE and net hydrogen binding energy of intermediate 2. The trend in the adiabatic ionization energy (AIE) and the net hydrogen binding energy of intermediate 2 for the [Ti₆Se₈(PMe₃)_{3-m}(CO)_m] (m = 0–3) cluster. The plot shows a smooth variation of both properties upon ligand substitution.

Ti₆Se₈(PMe₃)₃ pathway compared to the Ti₆Se₈(CO)₃ pathway (-0.26 |e|). The rest of the two clusters show intermediate charges on CO₂ and also follow the expected trend (see Supplementary Table 9). Apart from facilitating the charge transfer, it is also observed that the ligand-induced shift alters the binding energy of H atoms as well. Figure 7 also shows the net H binding energies (i.e., the binding energy of the H atom pair with the ligated cluster) for all four intermediates (2), and as shown, increasing the number of PMe₃ ligands results in a reduction of the same. According to our calculation, the net H binding energy has reduced monotonically from 3.45 eV to 3.26 eV as we move from [Ti₆Se₈(CO)₃H₂] to [Ti₆Se₈(PMe₃)₃H₂] cluster. One possible explanation for such reduction is that as the electronic spectrum shifts upward, the bonding orbitals of the attached hydrogens get energetically destabilized, thereby facilitating their release from the cluster surface. In other words, the upward shifting of the electronic (MO) spectrum along with the H bonding molecular orbitals results in the weakening of the bond and, thereby, the binding energy with the cluster. To summarize, we can conclude that the ligand-induced upward shifting of the electronic spectrum assists the H release from the cluster surface and also expedites the charge transfer from the cluster to CO₂ by improving the orbital overlap and reducing the ionization energy. Since the overall ligand-induced alteration of the H binding energy is smaller compared to the AIE, we think that the facilitation of the charge transfer due to the donor ligand attachment plays a dominant role in the observed barrier height reduction. Therefore, controlling the degree of the shift via ligands, as shown in this article, provides a way to predictably alter the barrier heights and hence the reactivity of the cluster.

Discussion

The present study provides valuable insight into how the rate of CO₂ conversion to formic acid can be controlled by attaching suitable combinations of donor/acceptor ligands to the Ti₆Se₈ cluster catalyst. Our investigation reveals that attaching σ-donor (e.g., PMe₃)/ π-acceptor (e.g., CO) ligands to the cluster induces an upward/downward shift of the electronic spectrum of the cluster without altering the sequence or the occupancy of the electronic levels. We have further shown that such ligand-induced alteration of the electronic levels also results in a change in the reactivity of the cluster in a predictable manner. This provides a unique opportunity to alter the barrier heights of the CO₂ conversion in a progressive and predictable manner simply by attaching different combinations of donor/acceptor ligands to the cluster. Analysis of our computational results reveals that the

alteration of the barrier is due to two different electronic effects. First, the upward shift of the electronic levels induced by the donor ligands lowers the ionization energy of the cluster and thereby facilitates the charge transfer toward CO₂. Second, the same shift also weakens the binding of H atoms to the cluster and hence assists the H-transfer process. While the present studies are based on Ti₆Se₈ clusters, the insight gained into the various mechanisms controlling the barrier should be applicable to other metal chalcogenide clusters as well. It is noteworthy that the influence of other donor/acceptor ligands and the effect of various solvents on the barrier heights remain as open questions that demand separate in-depth studies. Despite the fact, as mentioned earlier, using synthetic chemical techniques, it is now possible to synthesize the ligated metal chalcogenide clusters in solutions. Therefore, we hope the present study will motivate experimental investigation into the facile synthesis of formic acid, thereby reducing the environmental CO₂ concentration and converting it into useful products using metal chalcogenide clusters.

Methods

Computational details. All the reported results in this paper are calculated by using the Amsterdam Density Functional (ADF) package⁵⁹. The gradient-corrected Perdew, Burke, and Ernzerhof (GGA-PBE) exchange-correlation functional is used for all computations⁶⁰. The Slater-type triple ζ basis sets with two polarization functions (TZ2P) and large frozen electron cores are used for all the elements^{61,62}. The frozen core orbitals are expressed in an auxiliary set of Slater-type basis functions that is different from the valence set. The scalar relativistic corrections are incorporated via the zero-order regular approximation (ZORA)^{63,64}. The Hessian-based quasi-Newton method, without any symmetry constraints, is utilized for all optimizations⁶⁵. To check the validity of the optimized structures, analytical frequency calculations^{66,67} are performed, and it is ensured that all the normal modes of vibrations for the minima structures are real and positive, whereas all the transition states are first-order saddle points having only one imaginary frequency with significant magnitude. To verify that the respective transition states are connected to the reported minima at the left and the right-hand side of the transition state, the intrinsic reaction coordinate (IRC) calculations⁶⁸ are also performed. Since the geometry of all the transition states remained similar even after ligand attachment, the IRC calculations are performed only for the pristine cluster. This is also due to the high computational costs associated with each IRC calculation. The dispersion correction is included via Grimme's DFT-D3 method with the Becke–Johnson damping⁶⁹. The natural bond orbital (NBO) calculations are performed with NBO 6.0 program⁵⁶ as implemented within ADF⁵⁹ package. It is also confirmed that the spin contamination errors associated with all the open shell systems are negligible and within a reasonable level. A wide range of spin multiplicities are investigated during all optimizations, including for all the species along the reaction pathways, and only the ground state structures were selected for all cases.

Data availability

The optimized cartesian coordinates of the transition state structures, relative energies, barrier heights, and Hirshfeld charges are given in the Supplementary Information. Any additional data reported here with are available from the corresponding authors upon reasonable request.

Received: 22 November 2022; Accepted: 7 March 2023;

Published online: 21 March 2023

References

- Rosa, E. A. & Dietz, T. Human drivers of national greenhouse-gas emissions. *Nat. Clim. Change* **2**, 581–586 (2012).
- Hardy, J. T. *Climate change: causes, effects, and solutions*. (John Wiley & Sons), (2003).
- Singh, G. et al. Emerging trends in porous materials for CO₂ capture and conversion. *Chem. Soc. Rev.* **49**, 4360–4404 (2020).
- MacDowell, N. et al. An overview of CO₂ capture technologies. *Energy Environ. Sci.* **3**, 1645–1669 (2010).
- Taheri Najafabadi, A. CO₂ chemical conversion to useful products: an engineering insight to the latest advances toward sustainability. *Int. J. Energy Res.* **37**, 485–499 (2013).
- Song, C. Global challenges and strategies for control, conversion and utilization of CO₂ for sustainable development involving energy, catalysis, adsorption and chemical processing. *Catal. Today* **115**, 2–32 (2006).

7. Ma, Z., Legrand, U., Pahija, E., Tavares, J. R. & Boffito, D. C. From CO₂ to formic acid fuel cells. *Ind. Eng. Chem. Res.* **60**, 803–815 (2020).
8. Moret, S., Dyson, P. J. & Laurency, G. Direct synthesis of formic acid from carbon dioxide by hydrogenation in acidic media. *Nat. Commun.* **5**, 1–7 (2014).
9. Weillhard, A., Argent, S. P. & Sans, V. Efficient carbon dioxide hydrogenation to formic acid with buffering ionic liquids. *Nat. Commun.* **12**, 1–7 (2021).
10. Reda, T., Plugge, C. M., Abram, N. J. & Hirst, J. Reversible interconversion of carbon dioxide and formate by an electroactive enzyme. *Proc. Natl Acad. Sci.* **105**, 10654–10658 (2008).
11. Saeidi, S. et al. Mechanisms and kinetics of CO₂ hydrogenation to value-added products: A detailed review on current status and future trends. *Renew. Sustain. Energy Rev.* **80**, 1292–1311 (2017).
12. Ye, R.-P. et al. CO₂ hydrogenation to high-value products via heterogeneous catalysis. *Nat. Commun.* **10**, 1–15 (2019).
13. Yang, H. et al. A review of the catalytic hydrogenation of carbon dioxide into value-added hydrocarbons. *Catal. Sci. Technol.* **7**, 4580–4598 (2017).
14. Saeidi, S. et al. Recent advances in CO₂ hydrogenation to value-added products—Current challenges and future directions. *Prog. Energy Combust. Sci.* **85**, 100905 (2021).
15. Bai, S.-T. et al. Homogeneous and heterogeneous catalysts for hydrogenation of CO₂ to methanol under mild conditions. *Chem. Soc. Rev.* **50**, 4259–4298 (2021).
16. Wiedner, E. S. & Linehan, J. C. Making a splash in homogeneous CO₂ hydrogenation: elucidating the impact of solvent on catalytic mechanisms. *Chem. Eur. J.* **24**, 16964–16971 (2018).
17. Nitopi, S. et al. Progress and perspectives of electrochemical CO₂ reduction on copper in aqueous electrolyte. *Chem. Rev.* **119**, 7610–7672 (2019).
18. Li, W. et al. A short review of recent advances in CO₂ hydrogenation to hydrocarbons over heterogeneous catalysts. *RSC Adv.* **8**, 7651–7669 (2018).
19. Corrigan, J. F., Fuhr, O. & Fenske, D. Metal chalcogenide clusters on the border between molecules and materials. *Adv. Mater.* **21**, 1867–1871 (2009).
20. Champsaur, A. M. et al. Two-dimensional nanosheets from redox-active superatoms. *ACS Cent. Sci.* **3**, 1050–1055 (2017).
21. Pinkard, A., Champsaur, A. M. & Roy, X. Molecular clusters: nanoscale building blocks for solid-state materials. *Acc. Chem. Res.* **51**, 919–929 (2018).
22. Roy, X. et al. Nanoscale atoms in solid-state chemistry. *Science* **341**, 157–160 (2013).
23. Yang, J. et al. Shape Matching in Superatom Chemistry and Assembly. *J. Am. Chem. Soc.* **142**, 11993–11998 (2020).
24. Gadjeva, N. A., Champsaur, A. M., Steigerwald, M. L., Roy, X. & Nuckolls, C. Dimensional Control of Assembling Metal Chalcogenide Clusters. *Eur. J. Inorg. Chem.* **2020**, 1245–1254 (2020).
25. Lee, C. H. et al. Ferromagnetic ordering in superatomic solids. *J. Am. Chem. Soc.* **136**, 16926–16931 (2014).
26. Chauhan, V., Reber, A. C. & Khanna, S. N. Metal chalcogenide clusters with closed electronic shells and the electronic properties of alkalis and halogens. *J. Am. Chem. Soc.* **139**, 1871–1877 (2017).
27. Chauhan, V., Reber, A. C. & Khanna, S. N. Transforming Ni₉Te₆ from electron donor to acceptor via ligand exchange. *J. Phys. Chem. A* **120**, 6644–6649 (2016).
28. Chauhan, V., Sahoo, S. & Khanna, S. N. Ni₉Te₆(PEt₃)₈C₆₀ is a superatomic superalkali superparamagnetic cluster assembled material (S³-CAM). *J. Am. Chem. Soc.* **138**, 1916–1921 (2016).
29. Reber, A. C., Chauhan, V. & Khanna, S. N. Symmetry and magnetism in Ni₉Te₆ clusters ligated by CO or phosphine ligands. *J. Chem. Phys.* **146**, 024302 (2017).
30. Liu, G. et al. Ligand Effect on the Electronic Structure of Cobalt Sulfide Clusters: A Combined Experimental and Theoretical Study. *J. Phys. Chem. C* **123**, 25121–25127 (2019).
31. Liu, G. et al. Tuning the electronic properties of hexanuclear cobalt sulfide superatoms via ligand substitution. *Chem. Sci.* **10**, 1760–1766 (2019).
32. Chauhan, V., Reber, A. C. & Khanna, S. N. Strong lowering of ionization energy of metallic clusters by organic ligands without changing shell filling. *Nat. Commun.* **9**, 1–7 (2018).
33. Reber, A. C., Bista, D., Chauhan, V. & Khanna, S. N. Transforming Redox Properties of Clusters Using Phosphine Ligands. *J. Phys. Chem. C* **123**, 8983–8989 (2019).
34. Jena, P. & Castleman, A. W. *Nanoclusters: a bridge across disciplines*. (Elsevier), (2010).
35. Walter, M. et al. A unified view of ligand-protected gold clusters as superatom complexes. *Proc. Natl Acad. Sci.* **105**, 9157–9162 (2008).
36. Pichugina, D. A., Kuz'menko, N. E. & Shestakov, A. F. Ligand-protected gold clusters: the structure, synthesis and applications. *Russ. Chem. Rev.* **84**, 1114 (2015).
37. Xu, W. W., Zeng, X. C. & Gao, Y. Application of electronic counting rules for ligand-protected gold nanoclusters. *Acc. Chem. Res.* **51**, 2739–2747 (2018).
38. Roach, P. J., Woodward, W. H., Castleman, A. W. Jr, Reber, A. C. & Khanna, S. N. Complementary active sites cause size-selective reactivity of aluminum cluster anions with water. *Science* **323**, 492–495 (2009).
39. Reber, A. C. & Khanna, S. N. Superatoms: electronic and geometric effects on reactivity. *Acc. Chem. Res.* **50**, 255–263 (2017).
40. Abreu, M. B., Powell, C., Reber, A. C. & Khanna, S. N. Ligand-induced active sites: reactivity of iodine-protected aluminum superatoms with methanol. *J. Am. Chem. Soc.* **134**, 20507–20512 (2012).
41. Luo, Z. et al. What determines if a ligand activates or passivates a superatom cluster? *Chem. Sci.* **7**, 3067–3074 (2016).
42. Peng, G., Sibener, S. J., Schatz, G. C., Ceyer, S. T. & Mavrikakis, M. CO₂ hydrogenation to formic acid on Ni (111). *J. Phys. Chem. C* **116**, 3001–3006 (2012).
43. Yan, G., Gao, Z., Zhao, M., Yang, W. & Ding, X. CO₂ hydrogenation to formic acid over platinum cluster doped defective graphene: A DFT study. *Appl. Surf. Sci.* **517**, 146200 (2020).
44. Sarma, P. J. et al. Tuning the transition barrier of H₂ dissociation in the hydrogenation of CO₂ to formic acid on Ti-doped Sn₂O₄ clusters. *Phys. Chem. Chem. Phys.* **23**, 204–210 (2021).
45. Kishimoto, F. et al. Remote control of electron transfer reaction by microwave irradiation: kinetic demonstration of reduction of bipyridine derivatives on surface of nickel particle. *J. Phys. Chem. Lett.* **10**, 3390–3394 (2019).
46. Pan, H. & Liu, K. Fermi-phase-induced interference in the reaction between Cl and vibrationally excited CH₃D. *Nat. Chem.* **14**, 545–549 (2022).
47. Aljabour, A. et al. Active sulfur sites in semimetallic titanium disulfide enable CO₂ electroreduction. *ACS Catal.* **10**, 66–72 (2019).
48. Hasan, M. R., Abd Hamid, S. B., Basirun, W. J., Suhaimy, S. H. M. & Mat, A. N. C. A sol-gel derived, copper-doped, titanium dioxide-reduced graphene oxide nanocomposite electrode for the photoelectrocatalytic reduction of CO₂ to methanol and formic acid. *RSC Adv.* **5**, 77803–77813 (2015).
49. Handoko, A. D. et al. Two-dimensional titanium and molybdenum carbide MXenes as electrocatalysts for CO₂ reduction. *Science* **23**, 101181 (2020).
50. Esrafil, M. D. & Dinparast, L. A DFT study on the catalytic hydrogenation of CO₂ to formic acid over Ti-doped graphene nanoflake. *Chem. Phys. Lett.* **682**, 49–54 (2017).
51. Hirshfeld, F. L. Bonded-Atom Fragments for Describing Molecular Charge Densities. *Theor. Chim. Acta* **44**, 129–138 (1977).
52. Kaufmann, S., Schwarzer, D., Reichardt, C., Wodtke, A. M. & Bünermann, O. Generation of ultra-short hydrogen atom pulses by bunch-compression photolysis. *Nat. Commun.* **5**, 1–5 (2014).
53. Comerford, D. W., Smith, J. A., Ashfold, M. N. & Mankelevich, Y. A. On the mechanism of H atom production in hot filament activated H₂ and CH₄/H₂ gas mixtures. *J. Chem. Phys.* **131**, 044326 (2009).
54. LaVerne, J. A. & Huestis, P. L. H Atom Production and reaction in the gamma radiolysis of thermally modified boehmite. *J. Phys. Chem. C* **123**, 21005–21010 (2019).
55. Kovács, T., Blitz, M. A. & Seakins, P. W. H-atom yields from the photolysis of acetylene and from the reaction of C₂H with H₂, C₂H₂, and C₂H₄. *J. Phys. Chem. A* **114**, 4735–4741 (2010).
56. Glendening, E. D., Landis, C. R. & Weinhold, F. NBO 6.0: Natural bond orbital analysis program. *J. Comput. Chem.* **34**, 1429–1437 (2013).
57. Liu, P., Choi, Y., Yang, Y. & White, M. G. Methanol synthesis from H₂ and CO₂ on a Mo₆S₈ cluster: a density functional study. *J. Phys. Chem. A* **114**, 3888–3895 (2010).
58. Liu, C. & Liu, P. Mechanistic study of methanol synthesis from CO₂ and H₂ on a modified model Mo₆S₈ cluster. *ACS Catal.* **5**, 1004–1012 (2015).
59. te Velde, G. et al. Chemistry with ADF. *J. Comput. Chem.* **22**, 931–967 (2001).
60. Perdew, J. P., Burke, K. & Ernzerhof, M. Generalized Gradient Approximation Made Simple. *Phys. Rev. Lett.* **77**, 3865–3868 (1996).
61. Van Lenthe, E. & Baerends, E. J. Optimized Slater-type basis sets for the elements 1–118. *J. Comput. Chem.* **24**, 1142–1156 (2003).
62. Chong, D. P., Van Lenthe, E., Van Gisbergen, S. & Baerends, E. J. Even-tempered slater-type orbitals revisited: From hydrogen to krypton. *J. Comput. Chem.* **25**, 1030–1036 (2004).
63. Lenthe, E., van, Snijders, J. G. & Baerends, E. J. The zero-order regular approximation for relativistic effects: The effect of spin-orbit coupling in closed shell molecules. *J. Chem. Phys.* **105**, 6505–6516 (1996).
64. Van Lenthe, E., Ehlers, A. & Baerends, E.-J. Geometry optimizations in the zero order regular approximation for relativistic effects. *J. Chem. Phys.* **110**, 8943–8953 (1999).
65. Fan, L. & Ziegler, T. Optimization of molecular structures by self-consistent and nonlocal density-functional theory. *J. Chem. Phys.* **95**, 7401–7408 (1991).
66. Bérces, A. et al. An implementation of the coupled perturbed Kohn-Sham equations: perturbation due to nuclear displacements. *Comput. Phys. Commun.* **100**, 247–262 (1997).
67. Jacobsen, H., Bérces, A., Swerhone, D. P. & Ziegler, T. Analytic second derivatives of molecular energies: a density functional implementation. *Comput. Phys. Commun.* **100**, 263–276 (1997).

68. Deng, L. & Ziegler, T. The determination of Intrinsic Reaction Coordinates by density functional theory. *Int. J. Quantum Chem.* **52**, 731–765 (1994).
69. Grimme, S., Ehrlich, S. & Goerigk, L. Effect of the damping function in dispersion corrected density functional theory. *J. Comput. Chem.* **32**, 1456–1465 (2011).

Acknowledgements

The authors gratefully acknowledge funding by the US Air Force Office of Scientific Research (AFOSR), Grant No. FA 9550-18-1-0511.

Author contributions

T.S. has carried out all the theoretical calculations. Both T.S. and S.N.K. have participated in the scientific discussion and preparation of the manuscript.

Competing interests

The authors declare no competing interests.

Additional information

Supplementary information The online version contains supplementary material available at <https://doi.org/10.1038/s42004-023-00851-3>.

Correspondence and requests for materials should be addressed to Turbasu Sengupta or Shiv N. Khanna.

Peer review information *Communications Chemistry* thanks the anonymous reviewers for their contribution to the peer review of this work.

Reprints and permission information is available at <http://www.nature.com/reprints>

Publisher's note Springer Nature remains neutral with regard to jurisdictional claims in published maps and institutional affiliations.



Open Access This article is licensed under a Creative Commons Attribution 4.0 International License, which permits use, sharing, adaptation, distribution and reproduction in any medium or format, as long as you give appropriate credit to the original author(s) and the source, provide a link to the Creative Commons license, and indicate if changes were made. The images or other third party material in this article are included in the article's Creative Commons license, unless indicated otherwise in a credit line to the material. If material is not included in the article's Creative Commons license and your intended use is not permitted by statutory regulation or exceeds the permitted use, you will need to obtain permission directly from the copyright holder. To view a copy of this license, visit <http://creativecommons.org/licenses/by/4.0/>.

© The Author(s) 2023